electronics

MDPI

Article

RBF Neural Network-Enhanced Adaptive Sliding Mode Control for VSG Systems with Multi-Parameter Optimization

Jian Sun [1,2], Chuangxin Chen [1,*] and Huakun Wei [1]

[1] College of Electrical and New Energy, China Three Gorges University, Yichang 443002, China; sunjian2009@ctgu.edu.cn (J.S.); 202308580121240@ctgu.edu.cn (H.W.)
[2] Hubei Provincial Engineering Research Center of Intelligent Energy Technology, Yichang 443002, China
* Correspondence: chuangxin@ctgu.edu.cn

Abstract

Virtual synchronous generator (VSG) simulates the dynamic characteristics of synchronous generator, offering significant advantages in flexibly adjusting virtual inertia and damping parameters. However, their dynamic stability is susceptible to constraints such as control parameter design, grid disturbances, and the intermittent nature of distributed power sources. This study addresses the degradation of transient performance in traditional sliding mode control for VSG, caused by insufficient multi-parameter cooperative adaptation. It proposes an adaptive sliding mode control strategy based on radial basis function (RBF) neural networks. Through theoretical analysis of the influence mechanism of virtual inertia and damping coefficient perturbations on system stability, the RBF neural network achieves dynamic parameter decoupling and nonlinear mapping. Combined with an integral-type sliding surface to design a weight-adaptive convergence law, it effectively avoids local optima and ensures global stability. This strategy not only enables multi-parameter cooperative adaptive regulation of frequency fluctuations but also significantly enhances the system's robustness under parameter perturbations. Simulation results demonstrate that compared to traditional control methods, the proposed strategy exhibits significant advantages in dynamic response speed and overshoot suppression.

Keywords: virtual synchronous generator; virtual inertia; damping coefficient; radial basis function neural network; sliding mode control

check for updates

Academic Editors: Tushar Kanti Roy and Aman Maung Than Oo

Received: 18 September 2025
Revised: 20 October 2025
Accepted: 29 October 2025
Published: 31 October 2025

Citation: Sun, J.; Chen, C.; Wei, H. RBF Neural Network-Enhanced Adaptive Sliding Mode Control for VSG Systems with Multi-Parameter Optimization. *Electronics* **2025**, *14*, 4309. https://doi.org/10.3390/electronics14214309

Copyright: © 2025 by the authors. Licensee MDPI, Basel, Switzerland. This article is an open access article distributed under the terms and conditions of the Creative Commons Attribution (CC BY) license (https://creativecommons.org/licenses/by/4.0/).

1. Introduction

As the global energy transition accelerates, the International Energy Agency (IEA) notes in its 2023 Renewable Energy Report that distributed energy resources (DER), represented by rooftop solar and community wind power, are becoming a key pillar of global decarbonization. While DER optimize the energy mix by connecting to distribution grids via grid-tied inverters, these traditional inverters possess negligible rotational inertia. This makes them ill-equipped to handle the dynamic demands on grid voltage and frequency caused by DER intermittency and fluctuating electricity consumption patterns [1,2].

Virtual synchronous generator (VSG) [3] can simulate the external characteristics of a synchronous generator, thereby providing grid support functions [4,5]. Compared to conventional synchronous generators, VSGs offer flexible adjustment of parameters such as virtual inertia and damping coefficient [6–9], making them extensively studied and applied in enhancing the transient stability of systems incorporating intermittent energy sources.

Numerous studies have been published on adaptive control of VSG parameters. For instance, reference [10–12] directly controls one or more parameters—such as inertia, damping coefficients and droop coefficient [13]—to enable adaptive adjustment of these parameters in response to system dynamics. References [14,15] improve the aforementioned adaptive algorithms. For instance, Reference [14] enhances the degree of freedom in parameter tuning by modifying the control structure and designing a new transfer function. Reference [15] employs a segmented smoothing transition function to ensure continuous and smooth inertia adaptation while eliminating secondary oscillations caused by abrupt changes. Alternatively, optimization algorithms such as those based on genetic algorithms [16–18] can be employed to optimize parameters. Incorporating controllability metrics [16], precise model load forecasting [17], and adaptive fuzzy reasoning [18] can enhance control accuracy and effectiveness. References [19,20] employ particle swarm optimization to optimize parameters, integrating adaptive algorithms to enhance the system's dynamic response. However, most of these studies base their adaptive parameter control on linear models and fixed-function mappings, which present challenges such as difficult parameter design, complex state identification, and high requirements for system information [21]. Therefore, to fully leverage the frequency support capability of VSG, Reference [21] improved the control loop using virtual impedance, simplifying control parameters and improving system dynamic performance and applicability. reference [22] introduced fuzzy control to optimize compensation for the power control term and designed fuzzy control rules for adaptive parameter adjustment, effectively enhancing system frequency stability. However, within complex power grid interconnection systems, these control strategies fail to address stability issues arising from external disturbances or parameter perturbations, resulting in poor adaptability [23].

To address the aforementioned issues, some researchers have introduced sliding mode control (SMC) into the control loop [24–27]. Leveraging the strong robustness of SMC, this approach effectively resolves system stability problems. This method enhances system robustness under parameter perturbations and external disturbances. Reference [23] designed an adaptive robust sliding mode control strategy by treating the equivalent inertia coefficient as an adaptive parameter within the equivalent rotor motion model of doubly fed wind turbines, thereby more effectively improving the system's dynamic performance. Reference [24] improved the VSG mathematical model using a fourth-order synchronous generator model of the valve and excitation systems, designing an adaptive terminal sliding mode control method. Reference [25] incorporated adaptive fuzzy control into the active power control loop of the sliding mode control-based VSG, employing fuzzy approximation for the switching term. This approach effectively reduced system oscillations and significantly mitigated power oscillations. Reference [26] employs adaptive sliding mode control for virtual inertia within a multi-virtual synchronous machine system to prevent frequency instability. However, while these approaches ensure stability, they fail to fully leverage the dynamic performance optimization potential offered by the VSG's multi-parameter adjustability.

In summary, existing VSG sliding mode control research has yet to develop effective countermeasures against the impact of multi-parameter perturbations (such as dynamic variations in virtual inertia J and damping coefficient D) on control performance. Furthermore, under complex operating conditions (e.g., load transients, intermittent fluctuations from distributed power sources, voltage sags), the coordination of parameter adaptive adjustments remains inadequate, limiting improvements in system dynamic performance. Concurrently, traditional control approaches either focus solely on fixed settings for individual parameters or, while incorporating adaptive mechanisms, fail to fully leverage the synergistic advantages of nonlinear mapping and robust control. This makes it challenging

to simultaneously ensure system stability and dynamic response speed during transient processes. To address these research gaps, this study proposes a novel multi-parameter adaptive cooperative control strategy centered on the core requirements of VSG multi-parameter cooperative control. It integrates the nonlinear mapping capability of RBF neural networks with the variable-structure robust characteristics of sliding mode control. Its core contributions and key research points are as follows: First, leveraging the approximation capability of RBF neural networks for complex nonlinear relationships, the strategy uses system frequency deviation and its rate of change as inputs to achieve real-time decoupling and dynamic adjustment of virtual inertia J and damping coefficient D. This resolves the adjustment lag caused by parameter coupling in traditional control systems. Second, an integral sliding surface and adaptive approach law are designed based on sliding mode control. This approach injects strong robustness into the system's transient process to withstand multi-parameter perturbations. Simultaneously, the approach law dynamically adjusts the RBF neural network weights, ensuring the global stability of the closed-loop system and establishing a dynamic compensation mechanism under multi-parameter perturbations. Third, establishing synergistic constraints for J and D parameters based on multi-dimensional stability metrics, including damping ratio, amplitude margin, and phase margin. This optimizes dynamic response performance while ensuring system stability boundaries, preventing the trade-off between stability and dynamics caused by single-parameter tuning. To validate the proposed strategy's effectiveness, subsequent steps will involve constructing simulation models using Matlab/Simulink (Version R2022b). Under typical operating conditions—such as sudden load changes, fluctuations in distributed power generation, and voltage sags—the control performance will be compared with traditional control methods and other adaptive control strategies. The analysis will focus on improvements in system frequency dynamic response speed, overshoot, and disturbance rejection capability, providing technical support for the stable operation of VSG in complex grid environments.

2. VSG Parameters Analysis and Tuning

2.1. VSG Mathematical Model and Improved Control

The virtual synchronous machine circuit topology and improved control principle are shown in Figure 1. In this figure, the DC-side voltage of the inverter is typically supplied by renewable energy sources (wind, solar) and their energy storage systems. The grid voltage phase angle is set to 0° and serves as the reference value, where U represents the grid phase voltage and E denotes the inverter output phase voltage. R_f, L_f, and C_f correspond to the inverter's filter resistor, filter inductor, and filter capacitor, respectively. L_g represents the grid-side reactor.

Simplifying the research subject to seek general principles, this paper sets the pole pairs number to 1 [28], making the electrical angular velocity strictly equivalent to the mechanical angular velocity. Based on this, the mathematical model of the virtual synchronous generator (VSG) is established as follows:

$$\begin{cases} P_0 - P_e - D(\omega - \omega_0)\omega_0 = J\omega_0 \frac{d\omega}{dt} \\ \theta = \int \omega dt \\ P_0 = P_{ref} + k_p(\omega_0 - \omega) \\ U_0 = U_{ref} + \frac{1}{k_q}(Q_{ref} - Q) \end{cases} \tag{1}$$

In the equation: J represents the virtual inertia, D is the damping coefficient, k_p denotes the active power-frequency droop control coefficient; θ characterizes the virtual power angle parameter in the electromagnetic coupling state; P_0 is the mechanical input power

reference value, P_e corresponds to the instantaneous value of electromagnetic output power, and P_{ref} is defined as the active power reference benchmark; ω and ω_0 respectively quantify the real-time rotor angular frequency and the rated operating condition reference value; Q represents the measured reactive output quantity, Q_{ref} is the reactive setpoint reference, and k_q describes the reactive-voltage droop characteristic; U_{ref} sets the output voltage reference benchmark, while U_0 corresponds to the no-load electromotive force characteristic.

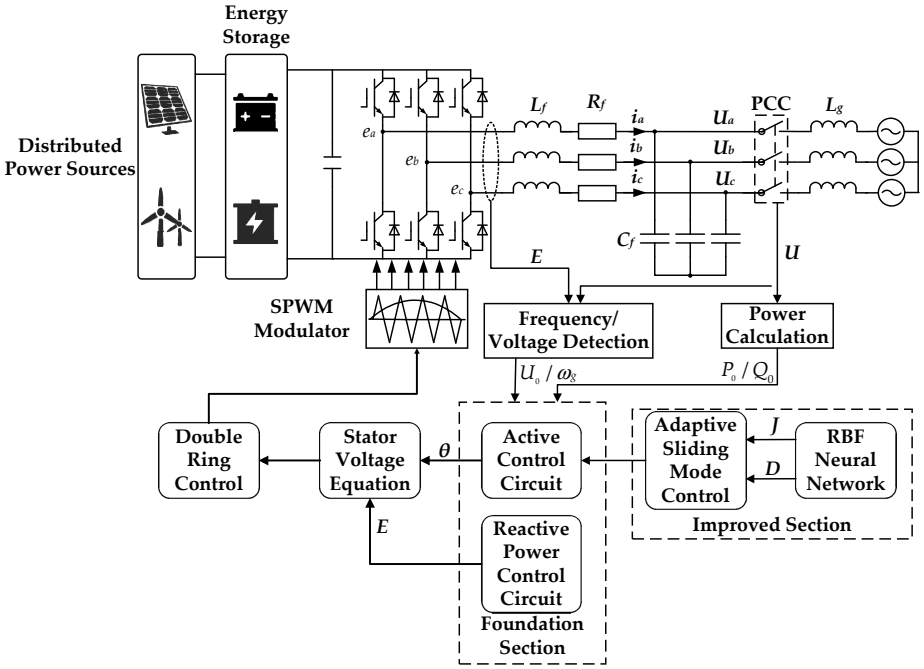


Figure 1. Schematic diagram of the improved VSG system.

The active and reactive power control block diagram is derived from the above system of Equation (1), as shown in Figure 2.

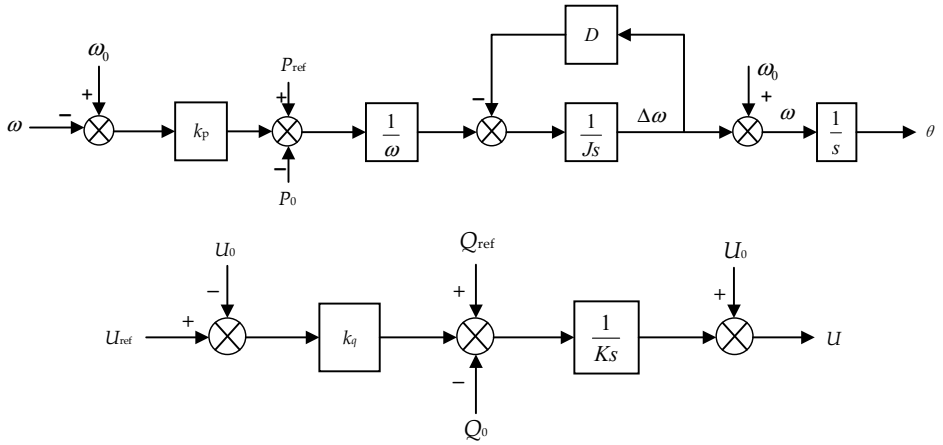


Figure 2. VSG control link.

2.2. VSG Stability Analysis and Parameter Perturbation Effects

Figure 3 shows the equivalent circuit model of a VSG grid-connected system [29]. Here, Z_f and Z_g represent the impedances of the inverter and grid, respectively, with $Z_f + Z_g = r + jX$, where r denotes the resistive component and X denotes the reactive component. Thus, $Z\angle\delta$ characterizes the equivalent output impedance of the VSG.

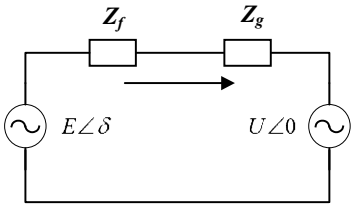


Figure 3. VSG grid-connected equivalent circuit.

During grid connection, as shown in Figure 3, the phase current of the line is:

$$\begin{cases} \dot{I} = \frac{E\angle\delta - U\angle 0}{Z} \\ Z = \sqrt{(\omega L)^2 + R^2} \\ \alpha = \arctan(\omega L / R) \end{cases} \tag{2}$$

where δ denotes the power angle of the virtual synchronous generator, Z represents the system equivalent impedance, and α is the equivalent impedance angle.

From the above equation, the VSG output power can be calculated as:

$$P_{\mathrm{e}} = \frac{3E_0U_l}{Z}\cos(\alpha - \delta) - \frac{3U_l^2}{Z}\cos\alpha \tag{3}$$

In actual power transmission and distribution systems, line impedance typically exhibits inductive characteristics [30]. Its resistive component can be neglected in practical engineering calculations, yielding $Xf \gg rf$. Thus, $\alpha \approx \pi/2$. Furthermore, small-signal analysis indicates that δ is very small. Therefore, the output power of the VSG can be approximated as:

$$P_{\mathrm{e}} = \frac{3E_0U_l}{X_f}\sin(\delta) \approx \frac{3E_0U_l}{X_f}\delta \tag{4}$$

By combining Equations (1) and (4), the simplified small-signal closed-loop control block diagram for the active-frequency control loop is shown in Figure 4.

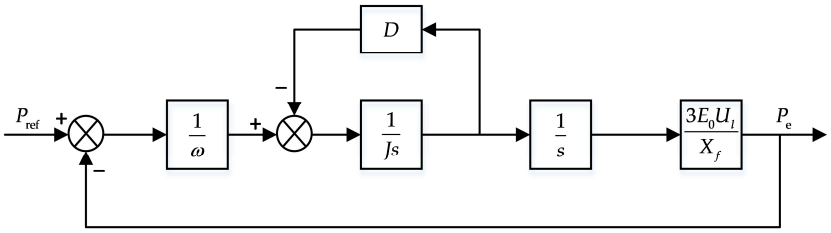


Figure 4. VSG small signal model.

From the small-signal model, we obtain a typical second-order system transfer function:

$$G(s) = \frac{\frac{3E_0U_l}{X_f}}{J\omega_0 s^2 + D\omega_0 s + \frac{3E_0U_l}{X_f}} \tag{5}$$

According to Equation (5), the corresponding dynamic characteristics parameters of the second-order system can be derived, including the undamped oscillation angular frequency ω_{n} and the damping ratio coefficient ξ.

$$\begin{cases} \omega_{\mathrm{n}} = \sqrt{\frac{3E_0U_l}{J\omega_0 X_f}} \\ \xi = D\sqrt{\frac{\omega_0 X_f}{12JE_0U_l}} \end{cases} \tag{6}$$

Analysis of the dynamic model established based on Equation (6) indicates that when the rotational inertia J is in the low-value range, excessive elevation of the damping coefficient D triggers the system to enter an over-damped state, resulting in a significant reduction in dynamic response rate. This phenomenon reveals a pronounced nonlinear relationship between the inertia J and the damping parameter D, necessitating global stability optimization during parameter tuning.

By plotting the root locus distribution of inertia-damping parameter variations in Figure 5, it can be observed that:

1. Damping Effect Under Fixed Inertia
   When J is constant, a sustained increase in D causes the system's dominant pole to migrate along an asymptote from the complex imaginary region in the left half-plane (under-damped oscillation mode) toward the negative real axis (evolving into over-damped behavior). This migration ultimately achieves full realization of the pole, satisfying the Marginal stability constraint.;
2. Inertia Effects Under Fixed Damping
   For typical damping values, as the inertia J increases, the absolute value of the pole's real part decreases while its imaginary part amplitude expands. This reflects that increased inertia reduces the system's undamped oscillation frequency.

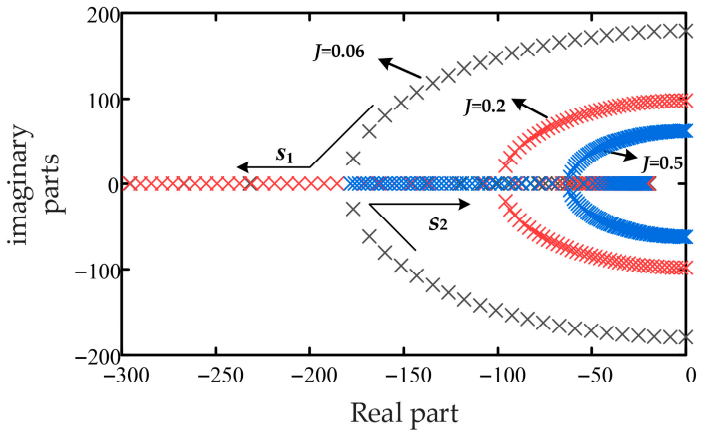


Figure 5. Root trajectories under different parameter variations.

Overall, the virtual inertia (J) and damping coefficient (D) significantly influence the dynamic response characteristics and stability margin of the VSG system. Increasing the virtual inertia enhances the system's frequency inertia support capability but leads to reduced transient response rates and increased power oscillation overshoot. Meanwhile, adjusting the damping coefficient directly affects the energy dissipation efficiency during transient processes.

2.3. Parameter Tuning

In the VSG parameter adaptive adjustment mechanism, the configuration of each control parameter plays a decisive role in system stability. Based on the dynamic characteristics of microgrid operating conditions, this paper proposes a coordinated tuning strategy for virtual inertia (J) and damping coefficient (D). Its stability analysis must satisfy the following prerequisites:

1. Active Power Output Limitation
The inverter is rated at 100 kVA, with its active power dynamic adjustment range constrained between 40% and 100% of the rated capacity [31]. The damping coefficient is influenced by both frequency variations and active power changes.

$$D = \frac{\Delta T}{\Delta \omega_{\max}} = \frac{\Delta P}{\omega \Delta \omega_{\max}} \approx \frac{\Delta P}{\omega_0 \Delta \omega_{\max}} \tag{7}$$

In the equation: ΔT represents the change in mechanical torque, where $\Delta T = \Delta P/\omega$, and ΔP denotes the change in active power; $\Delta\omega_{max}$ represents the maximum change in angular frequency.

2. Damping ratio constraints.
To ensure the amplitude of transient frequency oscillations in the power system remains within safe thresholds and maintains dynamic stability, the system damping ratio ξ must satisfy $0.612 < \xi < 1$. The damping ratio constraint is met when the parameters satisfy the following amplitude margin and phase margin requirements.

$$\begin{cases} h(\mathrm{dB}) = \frac{\omega\sqrt{\omega^2+4\xi^2\omega_n^2}}{\omega_n^2}|_{\omega=\omega_g} = +\infty \\ \gamma = \arctan\frac{2\xi\omega_n}{\omega}|_{\omega=\omega_c} = \arctan(\frac{2\xi}{\sqrt{\sqrt{1+4\xi^2}-2\zeta^2}}) > 60^\circ \end{cases} \tag{8}$$

3. Adjust the time limit.
According to the pole placement theory for second-order linear systems, as the absolute value of the negative real part of the underdamped closed-loop poles increases, shorter adjustment times result in less impact on system dynamics. Therefore, the real part of the closed-loop poles in this paper must satisfy:

$$\mathrm{Re}(s_i) = -\xi\omega_n \leq -10 \tag{9}$$

4. Cutoff Frequency Limitation
In the active power control loop, when the system operates at the gain crossover frequency, the open-loop transfer function's amplitude-frequency response satisfies the amplitude balance condition:

$$\left|G_p(j\omega_c) = 1\right| \tag{10}$$

From the closed-loop transfer function in Equation (5), the open-loop transfer function for active power is:

$$G_p(s) = \frac{3E_0U_l/\omega_0X_f}{Js^2 + Ds} \tag{11}$$

From the two equations, we obtain:

$$J = \frac{\sqrt{k^2 - D^2\omega_c^2}}{\omega_c^2} \tag{12}$$

Here, $k = 3E_0U_l/X_f\omega_0$, and $w_c = 2\pi f_c$. To ensure the existence of Equation (12), the expression under the square root must be non-negative, yielding:

$$f_c \leqslant \frac{3E_0U_l}{2\pi X_f\omega_0 D} \tag{13}$$

From the above constraints, the range of J is (0.035, 0.5), and the range of D is (15, 27.45).

3. Analysis of the Effect of Parameter Perturbation on Sliding Mode Control Performance

3.1. Equivalent State Space Equation

To refine the study of the effects of virtual inertia J and damping coefficient D on the sliding mode control strategy, the second-order rotor motion equations of a virtual synchronous motor are simplified using a small-signal model:

First, differentiate the first equation in (1) and simplify to obtain:

$$\dot{P}_{\mathrm{e}} = \omega_0\left(-D\dot{\omega} - J\ddot{\omega}\right) \tag{14}$$

Differentiating Equation (4) and combining it with Equation (14) yields the equivalent rotor motion equation:

$$k\dot{\delta} + J\ddot{\omega} + D\dot{\omega} = 0 \tag{15}$$

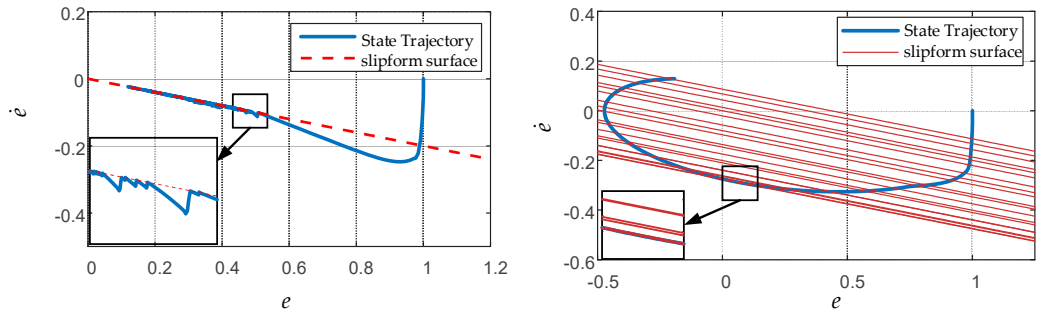
Among these, $k = 3E_0U_l / X_f\omega_{\mathrm{n}}$

Since virtual synchronous generator may be subject to uncertain disturbances in addition to parameter perturbations, let w denote the various uncertain disturbances in the system. Moreover, w is constrained by multiple physical limitations: the law of energy conservation dictates the theoretical upper bound of disturbance power, the rated parameters of power electronic devices impose hardware constraints, and system protection mechanisms define engineering boundaries. Consequently, the disturbance amplitude must satisfy the boundedness condition $|w| \leq \mathrm{W}$, where W is assumed to be a constant representing the maximum disturbance intensity. With an additional control input $u(t)$, the state variable set is defined as $X = \{x1,\ x2\}$, where $x_1 = \dot{\delta} = w$, $x_2 = \dot{\omega}$. Thus, the aforementioned equivalent rotor motion equation can be formulated as the stabilization problem for the following second-order uncertain nonlinear system:

$$\begin{cases} \dot{x}_1 = x_2 \\ \dot{x}_2 = \frac{1}{J}(-kx_1 - Dx_2 + w + u) \end{cases} \tag{16}$$

3.2. Sliding Mode Control Function Design

Define the tracking error as $e = x_1 - x_d$, so $\dot{e} = x_2 - \dot{x}_d$, x_d is the system's rated angular frequency. The integral sliding surface incorporates an error integral term $\lambda^2 \int e\mathrm{d}t$ to "accumulate the error signal," forcing the controller output to generate stronger correction signals. This ensures the error e strictly converges to zero, thereby eliminating steady-state error. Furthermore, the memory effect of the integral term in the integral sliding surface significantly enhances disturbance rejection capability. Compared to traditional sliding surfaces, the integral sliding surface exhibits smooth spiral convergence, effectively reducing chattering amplitude, as shown in Figure 6.



(**a**) (**b**)

Figure 6. (**a**) Traditional slipform facade plane; (**b**) Integral-type sliding surface facing plane.

Therefore, the following integral-type sliding surface is adopted to mitigate the impact of tracking error.

$$s = \dot{e} + 2\lambda e + \lambda^2 \int e\mathrm{d}t \tag{17}$$

where λ is the sliding surface parameter and is greater than 0. Setting $s = \dot{s} = 0$ yields the ideal sliding mode state:

$$s = \dot{s} = \ddot{e} + 2\lambda\dot{e} + \lambda^2 e = 0 \tag{18}$$

From Equation (18), it can be seen that when the time variable $t \to \infty$, the system tracking error $e \to 0$, and the tuning factor λ can optimize the quality of the dynamic response. Under idealized parameter conditions (i.e., when the inertia J and damping coefficient D are known quantities), substituting the dynamic equation and error function from Equation (16) into Equation (18) yields the ideal control law expression for the system:

$$u^* = J[\ddot{x}_d - 2\lambda\dot{e} - \lambda^2 e] + kx_1 + Dx_2 \tag{19}$$

3.3. Effect of Parameter Perturbation

Define the Lyapunov function as:

$$V = \frac{1}{2}Js^2 \tag{20}$$

Taking the derivative of Equation (20) yields:

$$\begin{aligned} \dot{V} &= sJ\dot{s} \\ &= s\left[u - kx_1 - Dx_2 + w - J(\ddot{x}_d - 2\lambda\dot{e} - \lambda^2 e)\right] \end{aligned} \tag{21}$$

To ensure $\dot{V} \leq 0$, the sliding mode control law can be designed as follows:

$$u = J[\ddot{x}_d - 2\lambda\dot{e} - \lambda^2 e] + kx_1 + Dx_2 - \eta_1 \mathrm{sgn}(s) \tag{22}$$

where $\eta_1 >$ W. Then:

$$\begin{aligned} \dot{V} &= s[-\eta \mathrm{sgn}(s) + w] \\ &= -\eta_1|s| + ws \end{aligned} \tag{23}$$

Let $\eta_1 \geq$ W+η_0 and $\eta_0 > 0$, then $\dot{V} \leq -\eta_0|s| \leq 0$. When $\dot{V} \equiv 0$, $s \equiv 0$. By LaSalle's invariant set principle, when $t \to \infty$, $s \to 0$. Furthermore, the convergence rate of s depends on η.

The disturbance synthesis term w described by Equation (23) encompasses dynamic uncertainties in the system. When the operating parameters of the VSG dynamically vary with frequency, the fluctuation amplitude of w exhibits nonlinear expansion characteristics.

To ensure control robustness, a sufficiently large disturbance upper bound W must be set. However, excessively large W values significantly increase the switching control gain η_1, leading to amplified sliding mode oscillations and degraded dynamic performance. Therefore, adaptive online adjustment of key VSG parameters is required to achieve the dual objectives of oscillation suppression and dynamic performance optimization.

4. Design of Adaptive Sliding Mode Control Strategy Based on RBF Neural Networks

4.1. RBF Neural Network Design

In the aforementioned sliding-mode variable-structure control, the failure to incorporate parameter adaptation not only leads to significant oscillation but also makes it challenging to determine the boundaries of uncertain disturbances in practical engineering applications. By leveraging the advantage of adaptive control—which modifies its own characteristics to accommodate changes in the dynamic properties of the controlled object and disturbances—the system can achieve superior control performance [23].

For VSG systems, since the primary parameters affecting system stability are the virtual inertia J and damping coefficient D, the design of control functions must address the adaptive adjustment of these two parameters. Furthermore, because parameter variations are not random perturbations but follow a specific pattern in response to system frequency changes, traditional adaptive sliding mode control with predefined upper and lower bounds becomes limited in this context.

RBF neural networks exhibit strong approximation capabilities for any nonlinear function, enabling adaptive adjustment of the aforementioned key parameters. By leveraging mechanisms such as local response, hidden layer feature extraction, nonlinear mapping, and hierarchical processing, RBF neural networks achieve decoupling of nonlinear input data [32]. Figure 7 illustrates the RBF neural network model:

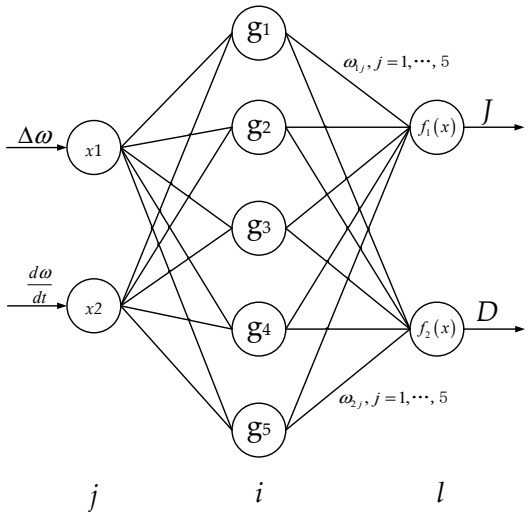


Figure 7. RBF neural network model.

The expression for the input layer of an RBF neural network is:

$$\dot{x} = \begin{bmatrix} x_1 & x_2 & \dots & x_n \end{bmatrix}^{\mathrm{T}} \tag{24}$$

The expression for the hidden layer of an RBF neural network is:

$$\begin{cases} h_j = \exp\left(\frac{\|x-c_j\|^2}{2b_j^2}\right), j = 1, 2, \ldots, m \\ \dot{c}_j = \begin{bmatrix} c_1 & c_2 & \ldots & c_m \end{bmatrix} \\ \dot{b} = \begin{bmatrix} b_1 & b_2 & \ldots & b_m \end{bmatrix}^{\mathrm{T}} \end{cases} \tag{25}$$

In the formula: j denotes the j-th neuron node in the hidden layer, h_j represents the output vector of the Gaussian kernel function. $\dot{c}_j$ is the center point vector value of the j-th hidden layer neuron, and $\dot{b}$ is the width vector of the Gaussian kernel function. m denotes the number of hidden layer nodes. In this paper, the number of nodes is set to 5. This quantity was initially determined using the empirical formula $h = \sqrt{n \times m} + a(a \in [1, 5])$, then refined through clustering algorithms such as K-Means to match the number of clusters. Finally, by balancing "fitting capability" and "generalization capability," it was confirmed that five hidden-layer nodes can achieve both sufficient fitting and stable generalization.

The output expression of an RBF neural network is:

$$y = \sum \omega_{lj} h_j, j = 1, 2, \ldots, m \tag{26}$$

where w_i denotes the output layer weight coefficient.

Based on dual-input feature vectors comprising system frequency deviation and frequency change rate, the rotational inertia J and damping coefficient D of the virtual synchronous generator are fitted in real-time via an RBF neural network. The output layer activation function is:

$$f(x) = \frac{u_i e^x}{e^x + e^{-x}}, i = 1, 2 \tag{27}$$

4.2. RBFA-SMC Strategy Design and Effectiveness Analysis

In the field of nonlinear system control, integrating sliding mode control (SMC) with RBF neural networks enables adaptive identification of unmodeled dynamic parameters through the RBF network. This approach significantly suppresses the impact of uncertainty terms w on the system, reduces the value of the fuzzy gain η, and avoids excessive oscillation amplitude caused by large switching gains [33].

In practical applications, the weights of RBF neural networks are often determined using gradient descent algorithms, which are prone to local optima and cannot guarantee global stability [34]. To coordinate the virtual inertia J and damping coefficient D while ensuring the stability and convergence of the entire closed-loop system, an adaptive law must be established to update the neural network weights, which introduces an estimation error. Therefore, let the estimated value and Prediction error of the virtual inertia J be denoted as $\hat{J}$ and $\widetilde{J}$, respectively, and the estimated value and Prediction error of the damping coefficient are denoted as $\hat{D}$d and $\widetilde{D}$, respectively. According to the RBF neural network algorithm:

$$\begin{cases} J(\cdot) = W^{*\mathrm{T}} h_J(x) + \varepsilon_J \\ D(\cdot) = V^{*\mathrm{T}} h_D(x) + \varepsilon_D \end{cases} \tag{28}$$

Among these, W^* and V^* represent the ideal weight matrices approximating the nonlinear functions $J(\cdot)$ and $D(\cdot)$, respectively. ε_J and ε_D characterize the network approximation errors, whose absolute values satisfy the boundary constraints $|\varepsilon_J| \leq \varepsilon_{MJ}$ and $|\varepsilon_D| \leq \varepsilon_{MD}$.

Defining the input vector as $x = [x1 \quad x2]^{\mathrm{T}}$, the mathematical output expression of the RBF neural network can be represented as:

$$\begin{cases} \hat{J}(x) = \hat{W}^{\mathrm{T}} h_J(x) \\ \hat{D}(x) = \hat{V}^{\mathrm{T}} h_D(x) \end{cases} \tag{29}$$

where $\hat{W}^{\mathrm{T}}$ is the estimated value of W^{*T}, and the estimation error of W^{T} is defined as $\widetilde{W}^{T}$, then $\widetilde{W}^{T} = \hat{W}^{T} - W^{*T}$ and $\widetilde{V}^{\mathrm{T}} = \hat{V}^{\mathrm{T}} - V^{*\mathrm{T}}$. Therefore:

$$\begin{cases} \widetilde{J} = \hat{J} - J = \hat{W}^{\mathrm{T}} h_J(x) - W^{*\mathrm{T}} h_J(x) - \varepsilon_J \\ \quad = \widetilde{W}^{\mathrm{T}} h_J(x) - \varepsilon_J \\ \widetilde{D} = \hat{D} - D = \hat{V}^{\mathrm{T}} h_D(x) - V^{*\mathrm{T}} h_D(x) - \varepsilon_D \\ \quad = \widetilde{V}^{\mathrm{T}} h_D(x) - \varepsilon_D \end{cases} \tag{30}$$

To address the requirement for suppressing the approximation error ε in neural networks, a robust compensation term u_2 is integrated into the control law design. The resulting control law is defined as $u = u_1 + u_2$:

$$\begin{cases} u_1 = \hat{J}[\ddot{x}_d - 2\lambda\dot{e} - \lambda^2 e] + kx_1 + \hat{D}x_2 \\ u_2 = -\eta \mathrm{sgn}(s) \end{cases} \tag{31}$$

where $\eta >$ M, and M is a constant.

Next, design the Lyapunov function as follows:

$$V = \frac{1}{2} J s^2 + \frac{1}{2\gamma_1} \widetilde{W}^{\mathrm{T}} \widetilde{W} + \frac{1}{2\gamma_2} \widetilde{V}^{\mathrm{T}} \widetilde{V} \tag{32}$$

where $\gamma_1 > 0$, $\gamma_2 > 0$.

Taking the derivative of Equation (32) yields:

$$\begin{aligned} \dot{V} &= sJ\dot{s} + \tfrac{1}{\gamma_1} \widetilde{W}^{\mathrm{T}} \dot{\widetilde{W}} + \tfrac{1}{\gamma_2} \widetilde{V}^{\mathrm{T}} \dot{\widetilde{V}} \\ &= s\big[u - kx_1 - Dx_2 - J(\ddot{x}_d - 2\lambda\dot{e} - \lambda^2 e)\big] + \\ &\quad \tfrac{1}{\gamma_1} \widetilde{W}^{\mathrm{T}} \dot{\hat{W}} + \tfrac{1}{\gamma_2} \widetilde{V}^{\mathrm{T}} \dot{\hat{V}} \\ &= \widetilde{V}^{\mathrm{T}} [s x_2 h_D(x) + \tfrac{1}{\gamma_2} \dot{\hat{V}}] + \\ &\quad \widetilde{W}^{\mathrm{T}} [s h_J(x)(\ddot{x}_d - 2\lambda\dot{e} - \lambda^2 e) + \tfrac{1}{\gamma_1} \dot{\hat{W}}] - \\ &\quad s[x_2 \varepsilon_D + \varepsilon_J(\ddot{x}_d - 2\lambda\dot{e} - \lambda^2 e) + \eta \mathrm{sgn}(s)] \end{aligned} \tag{33}$$

The following adaptive law is adopted:

$$\begin{cases} \dot{\hat{W}} = -\gamma_1 s h_J(x)(\ddot{x}_d - 2\lambda\dot{e} - \lambda^2 e) \\ \dot{\hat{V}} = -\gamma_2 s h_D(x) x_2 \end{cases} \tag{34}$$

Therefore:

$$\begin{aligned} \dot{V} &= -s[\varepsilon_D \dot{e} + \varepsilon_J(\ddot{x}_d - 2\lambda\dot{e} - \lambda^2 e) + \eta \mathrm{sgn}(s)] \\ &= (-\varepsilon_D \dot{e} - \varepsilon_J(\ddot{x}_d - 2\lambda\dot{e} - \lambda^2 e))s - \eta|s| \end{aligned} \tag{35}$$

Since the approximation errors ε_J and ε_D of the RBF network are very small real numbers, setting $\eta \geq \varepsilon_{MD}\dot{e} + \varepsilon_{MJ}(\ddot{x}_d - 2\lambda\dot{e} - \lambda^2 e) + \eta_0$, $\eta_0 > 0$ yields $\dot{V} \leq -\eta_0|s| \leq 0$. When $\dot{V} \equiv 0$, $s \equiv 0$. According to LaSalle's invariant set principle, when $t \to \infty$, $s \to 0$.

Finally, the block diagram of the neural network adaptive sliding mode control strategy proposed in this paper, RBFA-SMC (radial basis function adaptive-sliding mode control), is shown in Figure 8.

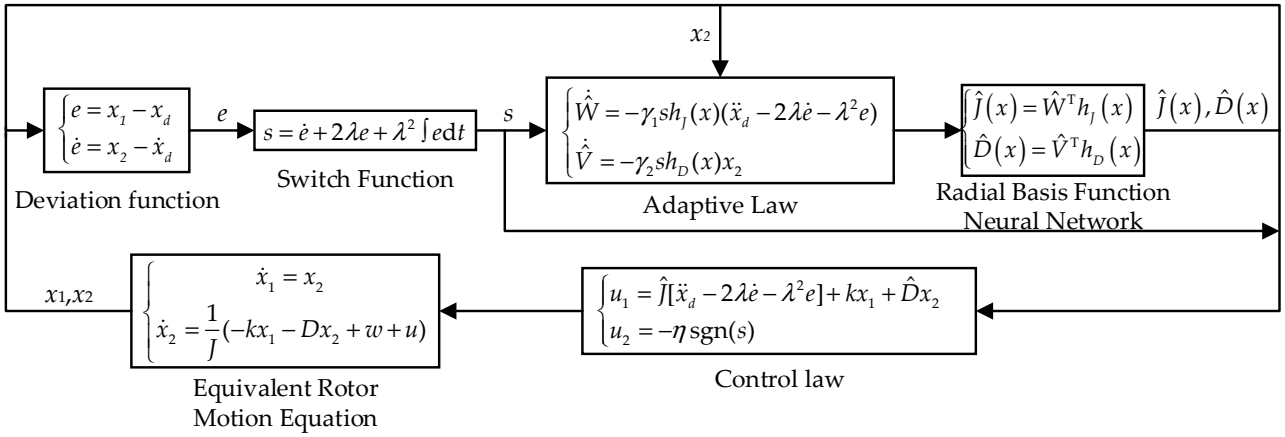


Figure 8. RBFA-SMC strategy structure diagram.

As shown in Equation (35), the approximation errors ε_J and ε_D in the RBF network cause the fuzzy gain η to be significantly smaller than η_1. This reduces system chatter and enhances dynamic performance. It is demonstrated that the virtual synchronous motor rotor motion system, whose multiple parameters are approximated by an RBF neural network, achieves asymptotic stability under the proposed sliding mode control law and adaptive law. The system frequency can track the desired rated synchronous angular frequency while mitigating the impact of system disturbances.

5. Simulation Analysis

To validate the effectiveness of the proposed RBFA-SMC strategy, a standard VSG grid-connected system model was constructed in the MATLAB/Simulink (Version R2022b) environment. Vertically, it is compared with traditional fixed-parameter control strategies (Fixed-JD) and the virtual inertia adaptive control strategy based on SMC (A-SMC). Horizontally, it is contrasted with particle swarm optimization-based adaptive control (IPOS) and adaptive fuzzy control (AFC). Validation was conducted under low-voltage ride-through, output fluctuation, and voltage sags conditions. Simulation parameters are shown in Table 1.

Table 1. Main parameters of the simulation model.

Title 1	Title 3
DC-side voltage U_{dc} (V)	750
Grid-side rated voltage U_g (V)	380
Rated frequency f_0 (Hz)	50
Rated angular frequency ω_0 (rad·s^{-1})	314
Grid-side equivalent resistance r_g (mΩ)	5
Grid-side equivalent inductance L_g (mH)	1.4
Equivalent resistance of filter circuit r_f (mΩ)	10
Filter Inductor L_f (mH)	0.6
Filter capacitor C (μF)	1500
Sliding mode parameter λ	1000
Sliding mode Parameter η	1.5

The AFC algorithm employs fuzzy logic control rules [22] to adaptively adjust the proportional (k_p) and derivative (k_d) coefficients based on frequency deviation $\Delta\omega$ and

frequency change rate $\Delta\dot{\omega}$, thereby optimizing frequency response in stages. Its core formula is:

$$\begin{cases} P_p = k_p \Delta\omega \\ P_d = -k_d \Delta\dot{\omega} \end{cases} \tag{36}$$

$$J\omega_0 \frac{d\omega}{dt} = P_{\text{ref}} - (P_e - P_p - P_d) + K_\omega(\omega_0 - \omega) + D\omega_0(\omega_0 - \omega) \tag{37}$$

Here, K_ω denotes the active droop coefficient. This method achieves flexible power coordination control between the renewable energy inverter and the VSG through the power regulation terms P_p and P_d generated by the virtual inertia controller.

The core formula [19] of the IPOS adaptive algorithm is:

$$\begin{cases} v_i^{n+1} = \omega v_i^n + c_1 Q_i (p_i^n - x_i^n) + c_2 Q_i (p_g^n - x_i^n) \\ x_i^{n+1} = x_i^n + v_i^{n+1} \end{cases} \tag{38}$$

where v_i^n and x_i^n denote the velocity and position of particle i at iteration n; p_i^n Pin represents the individual optimal position of particle i; p_g^n indicates the population's optimal position. With a population size of 50 and a maximum iteration count of 100, the steady-state values of the moment of inertia and damping coefficient are obtained via the aforementioned formula. Transient intervals are then defined based on the frequency deviation $\Delta\omega$ and frequency change rate $\Delta\dot{\omega}$, enabling adaptive adjustment of J and D. The adaptive formulas [19] are as follows:

$$J = \begin{cases} J_0 - k_1 \left(\left| \frac{df}{dt} \right| \right)^{m_1}, \left| \frac{df}{dt} \right| > N_J \cap \Delta\omega \frac{df}{dt} < 0 \cap J > J_{min} \\ J_{min}, \left| \frac{df}{dt} \right| > N_J \cap \Delta\omega \frac{df}{dt} < 0 \cap J \le J_{min} \\ J_0 + k_1 \left(\left| \frac{df}{dt} \right| \right)^{m_1}, \left| \frac{df}{dt} \right| > N_J \cap \Delta\omega \frac{df}{dt} > 0 \cap J < J_{max} \\ J_{max}, \left| \frac{df}{dt} \right| > N_J \cap \Delta\omega \frac{df}{dt} > 0 \cap J < J_{max} \\ J_0, \left| \frac{df}{dt} \right| < N_J \end{cases} \tag{39}$$

$$D = \begin{cases} D_{min}, \left| \frac{df}{dt} \right| > N_D \cap \Delta\omega \frac{df}{dt} > 0 \cap D \le D_{min} \\ D_0 \sqrt{1 - \frac{1}{J_0} k_2 \left(\left| \frac{df}{dt} \right| \right)^{n_1}}, \left| \frac{df}{dt} \right| > N_D \cap \Delta\omega \frac{df}{dt} > 0 \cap D > D_{min} \\ D_0 \sqrt{1 + \frac{1}{J_0} k_2 \left(\left| \frac{df}{dt} \right| \right)^{n_1}}, \left| \frac{df}{dt} \right| > N_D \cap \Delta\omega \frac{df}{dt} < 0 \cap D < D_{max} \\ D_{max}, \left| \frac{df}{dt} \right| > N_D \cap \Delta\omega \frac{df}{dt} < 0 \cap D \ge D_{max} \\ D_0, \left| \frac{df}{dt} \right| < N_D \end{cases} \tag{40}$$

where J_0 and D_0 represent the steady-state values of J and D; k_1 and k_2 denote proportional coefficients; m_1 and m_2 denote exponential coefficients; $J_{\max}$ and $J_{\min}$ denote the maximum and minimum values of J; $D_{\max}$ and $D_{\min}$ denote the maximum and minimum values of D; N_J and N_D denote the frequency variation thresholds.

5.1. Simulation Analysis Under the Condition of Output Fluctuation

To simulate the intermittent nature of distributed power sources, such as the sudden surge in output caused by strong winds during wind power generation. The simulation duration is 1 s, with an initial output of 50 kW that abruptly increases to 100 kW at 0.6 s, while reactive power remains constant. Figure 9a illustrates the angular frequency response under three control strategies. The traditional Fixed-*JD* strategy exhibits the largest frequency overshoot (M_{p1} = 0.55%) and longest transient recovery time (t_{s1} = 0.25 s) due to its fixed parameters; The ASMC-*J* strategy reduces overshoot to 0.39% (M_{p2}) and shortens recovery time to 0.20 s (t_{s2}) through adaptive adjustment of J. The proposed

RBFA-SMC strategy further suppresses frequency fluctuations, achieving overshoot as low as 0.17% (M_{p3}) and a recovery time of only 0.14 s (t_{s3}).

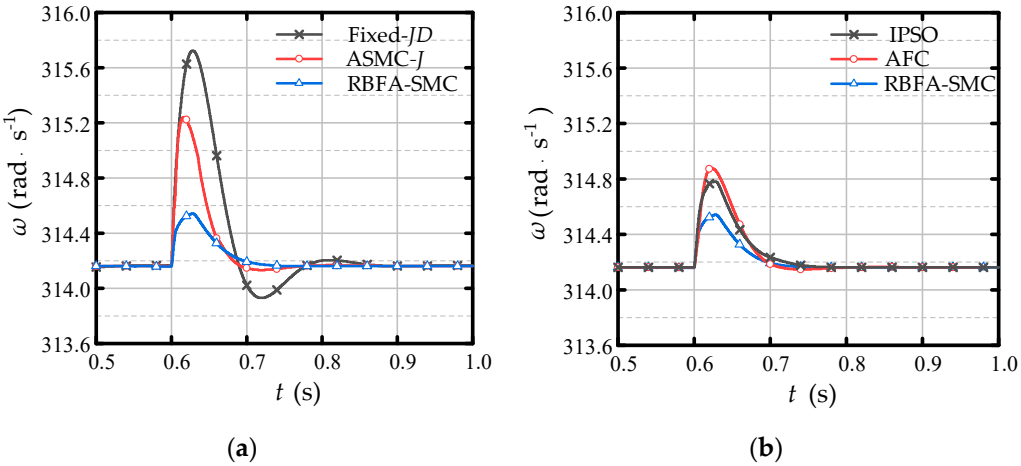


Figure 9. Comparison of angular frequency response under fluctuating output conditions. (**a**) Longitudinal Comparison; (**b**) Cross-sectional Comparison.

As shown in Figure 9a, compared with the traditional Fixed-*JD* strategy and the ASMC-*J* strategy, the proposed RBFA-SMC strategy achieves shorter frequency deviations and faster transient recovery times. It adaptively adjusts the virtual inertia and damping coefficient to suppress abrupt frequency increases during the rise phase and accelerate frequency recovery during the fall phase. This enables real-time online adjustment of the VSG frequency. Furthermore, by leveraging sliding mode control characteristics, the strategy ensures the system remains in a globally stable state, maintaining the frequency within a stable range.

As shown in Figure 9b, the IPOS adaptive algorithm, AFC algorithm, and the RBFA-SMC strategy proposed in this paper all exhibit relatively stable dynamic responses to angular frequency fluctuations under output power variations. They ensure smooth transitions in the angular frequency response curves. However, the RBFA-SMC strategy demonstrates superior performance in terms of both frequency overshoot magnitude and recovery time.

Table 2 compares the dynamic responses of active power. The Fixed-*JD* strategy exhibits a power overshoot of 7.6% (ΔP_1 = 7.67 kW), while the ASMC-*J* strategy reduced it to 4.6% (ΔP_2 = 4.60 kW). The RBFA-SMC strategy, leveraging the robustness of sliding mode control, controlled the overshoot to 0.7% (ΔP_3 = 0.77 kW), with a smooth power curve free of oscillations.

Table 2. Indicators for analyzing different control strategies under output fluctuations.

Control Strategy	ΔP_{max} (kW)	$\Delta\omega_{max}$ (rad·s^{-1})	t_s (s)
Fixed-*JD*	7.67	1.57	0.25
ASMC-*J*	4.60	1.09	0.20
AFC	1.22	0.72	0.18
IPSO	0.69	0.63	0.16
RBFA-SMC	0.77	0.39	0.14

As shown in the active power output waveform in Figure 10a, compared with the traditional Fixed-*JD* strategy and ASMC-*J* strategy, the RBFA-SMC strategy exhibits smoother active power variations under output fluctuations. It achieves a steady state faster while ensuring smaller overshoot. Furthermore, the figure demonstrates that the RBFA-SMC

curve exhibits smaller oscillation amplitude than the conventional adaptive sliding mode control while achieving superior transient performance.

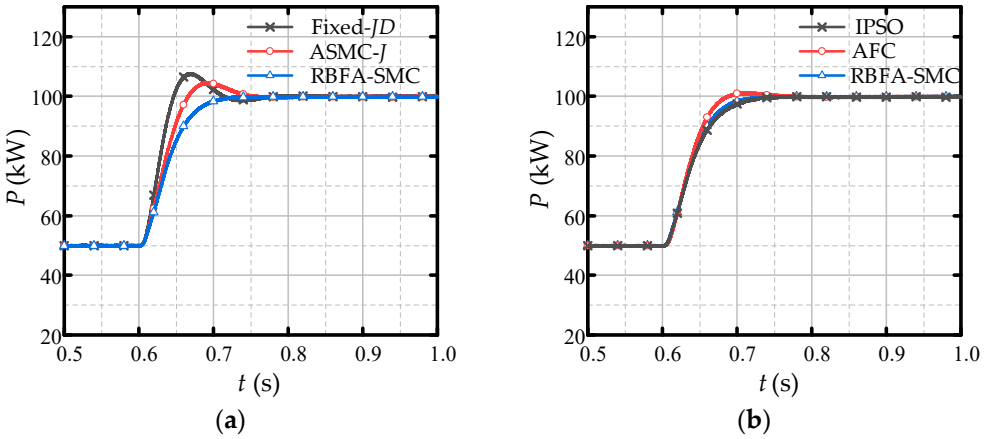


Figure 10. Comparison of active power response under fluctuating output conditions. (**a**) Longitudinal comparison; (**b**) Cross-sectional comparison.

As shown in Figure 10b, the IPOS adaptive algorithm, AFC algorithm, and RBFA-SMC strategy exhibit smoother active power fluctuations under intermittent output variations from renewable energy sources. They prevent significant oscillations during transient states and achieve a smooth transition to the steady-state phase. Among these, the RBFA-SMC strategy proposed in this paper demonstrates greater stability during transient processes, with reduced overshoot and shorter transient times.

Figure 11 illustrates the dynamic variations in the virtual inertia (J) and damping coefficient (D) in the RBFA-SMC strategy. During output fluctuations, both parameters undergo real-time adjustments within reasonable ranges under RBF neural network adaptive sliding mode control. This effectively suppresses high-frequency oscillations triggered by fuzzy gain switching, thereby reducing the amplitude of transient fluctuations in the VSG output frequency and active power. Consequently, the system recovery time to steady state is further shortened.

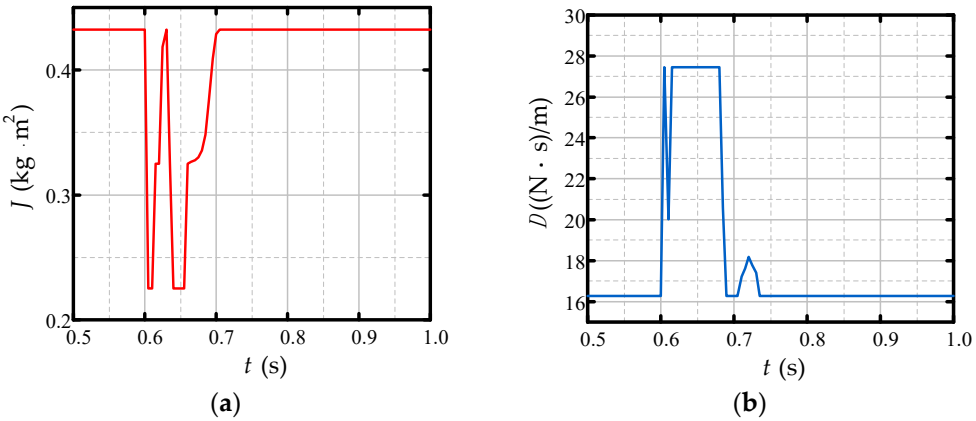


Figure 11. Under fluctuating output conditions. (**a**) Real-time value of J; (**b**) Real-time value of D.

5.2. Simulation Analysis of Low-Frequency Ride-Through Conditions

When transient grid faults or fluctuating user loads cause momentary frequency dips, to validate the effectiveness of the proposed control strategy under such typical operating conditions, the traditional Fixed-JD strategy, ASMC-J strategy, IPOS adaptive algorithm and AFC algorithm are also employed for comparative verification. The dynamic response of the simulated system during low-frequency ride-through scenarios is analyzed. The

simulation modeled a grid frequency fluctuation where the frequency dropped by 0.1 Hz at 0.2 s after load injection and recovered at 0.3 s. All other parameters remained constant throughout the simulation.

Figure 12a shows that the Fixed-*JD* strategy exhibits a frequency deviation of 0.60 rad/s after frequency recovery, with a recovery time of 0.25 s (t_{s4}); The ASMC-*J* strategy reduces the frequency deviation to 0.33 rad/s with a recovery time of 0.21 s (t_{s5}); The RBFA-SMC strategy achieves a frequency deviation of only 0.16 rad/s through the synergistic effect of dynamic compensation and sliding mode control, with the recovery time shortened to 0.17 s (t_{s6}).

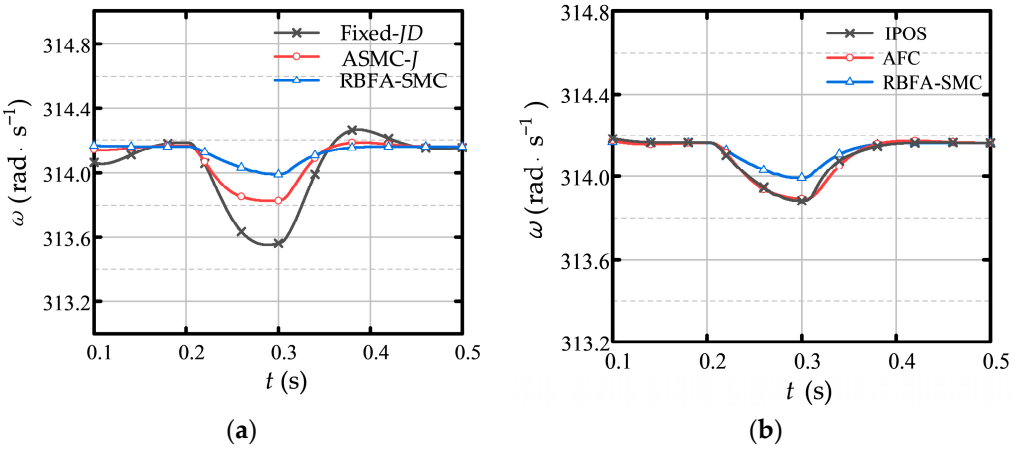


Figure 12. Comparison of angular Frequency Response under Low-Frequency ride-through Conditions. (**a**) Longitudinal comparison; (**b**) Cross-sectional comparison.

It can be observed that when grid frequency declines, the VSG frequency also decreases. However, compared to the traditional Fixed-*JD* strategy and ASMC-*J* strategy, the RBFA-SMC strategy exhibits smaller frequency deviation and a lower rate of frequency change during the frequency decline phase, demonstrating a significant damping effect on frequency drop. During the frequency recovery phase, the frequency curve is smoother, stability is higher, and recovery is faster.

Comparing the angular frequency responses under low-frequency ride-through conditions in Figure 12b reveals that the transient recovery times for the IPOS adaptive algorithm, AFC algorithm, and RBFA-SMC strategy are all around 0.17 s. However, during the frequency decline phase, the RBFA-SMC strategy most effectively suppresses frequency drop but exhibits slight oscillations. In the frequency recovery phase, the IPOS adaptive algorithm achieves the fastest recovery speed. The AFC algorithm exhibits greater stability in its curve performance and smoother transitions.

Table 3 compares the dynamic responses of active power under low-frequency ride-through conditions for the Fixed-*JD* strategy, ASMC-*J* strategy, and RBF-SMC strategy. After frequency restoration, the power overshoot of the Fixed-*JD* strategy reached 4.7% (ΔP_1 = 2.38 kW), while the ASMC-*J* strategy reduced it to 3.5% (ΔP_2 = 1.78 kW). Leveraging the robustness of sliding mode control, the RBF-SMC strategy controlled the overshoot to 0.6% (ΔP_3 = 0.30 kW), with a smooth power curve exhibiting no oscillations.

Table 3. Indicators for analyzing different control strategies under low-frequency ride-through conditions.

Control Strategy	ΔP_{max} (kW)	$\Delta\omega_{max}$ (rad·s^{-1})	t_s (s)
Fixed-*JD*	2.38	0.60	0.25
ASMC-*J*	1.78	0.33	0.21
AFC	1.03	0.26	0.18
IPSO	0.74	0.27	0.17
RBFA-SMC	0.30	0.16	0.17

As shown in Figure 13a, all three control strategies increased power output to counteract the frequency drop after the grid frequency decline. Among them, the RBFA-SMC strategy generated the highest additional power, more effectively suppressing grid frequency fluctuations. After grid frequency recovery, compared to the Fixed-*JD* and ASMC-*J* strategies, the RBFA-SMC strategy returned to a stable active power output state with a faster and more stable curve. Compared to the other two control strategies, it exhibited shorter active power recovery time and smaller active power fluctuation amplitude.

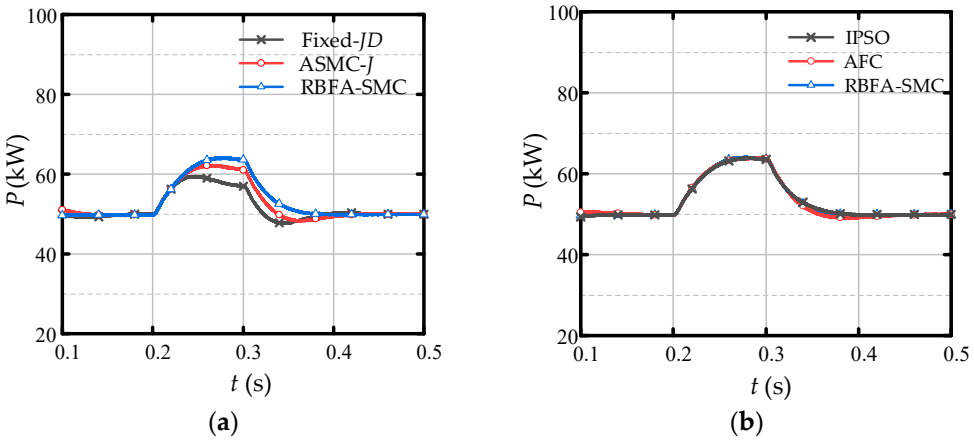


Figure 13. Comparison of active power response under low-frequency ride-through conditions. (**a**) Longitudinal comparison; (**b**) Cross-sectional comparison.

Comparing the active power responses under low-frequency ride-through conditions in Figure 13b, the active power curves of the IPOS adaptive algorithm, AFC algorithm, and RBFA-SMC strategy are nearly identical. All three approaches provide stable active power support during grid frequency drops, ensuring the system frequency recovers to its rated state as quickly as possible.

Figure 14 illustrates the dynamic variations in virtual inertia J and damping coefficient D under the RBFA-SMC strategy during system frequency transients. When grid frequency drops, the RBF neural network dynamically optimizes J and D based on the adaptive law, effectively damping oscillations triggered by parameter perturbations. This reduces the amplitude of transient fluctuations in VSG output frequency and active power, further shortening the system's recovery time to steady state.

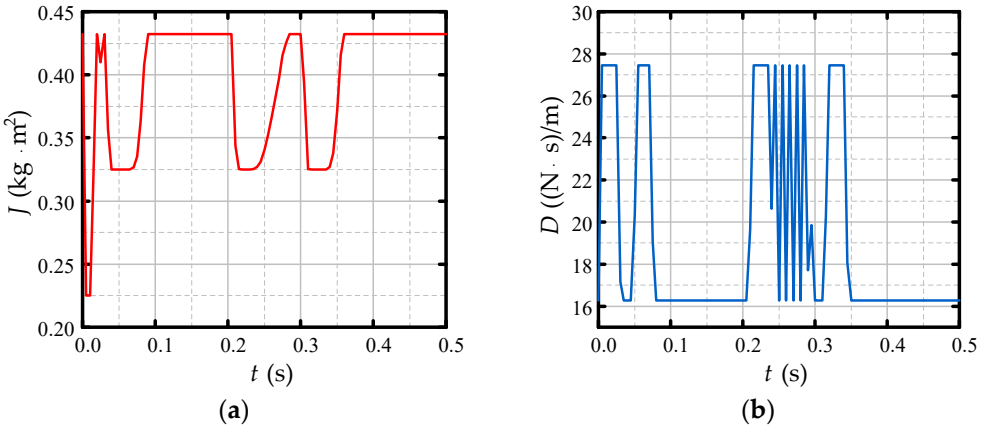


Figure 14. Under low-frequency ride-through conditions. (**a**) Real-time value of J; (**b**) Real-time value of D.

5.3. Simulation Analysis Under Voltage Sag Conditions

When faults such as short circuits occur in the power grid, grid voltage drops significantly. This poses a challenge for the entire power system. To ensure that renewable energy sources can continue supporting the grid during voltage sags without causing instability, the effectiveness of the proposed control strategy under these conditions is verified. For comparison, traditional Fixed-*JD* control, A-SMC, IPOS adaptive control, and AFC strategies are employed to simulate the dynamic response of the system during voltage sags. The simulation modeled a grid voltage drop to 50% of its original value at 0.2 s, with recovery occurring at 0.3 s. All other parameters remained constant throughout the simulation.

Figure 15a shows that the Fixed-*JD* strategy exhibits a maximum frequency deviation of 3.19 rad/s during the voltage dip phase, with a recovery time of 0.36 s (t_{s7}); The A-SMC strategy reduced frequency deviation to 1.46 rad/s with a recovery time of 0.32 s (t_{s8}); The RBFA-SMC strategy, through the synergistic effect of dynamic compensation and sliding mode control, achieved a frequency deviation of only 0.43 rad/s and shortened the recovery time to 0.22 s (t_{s9}).

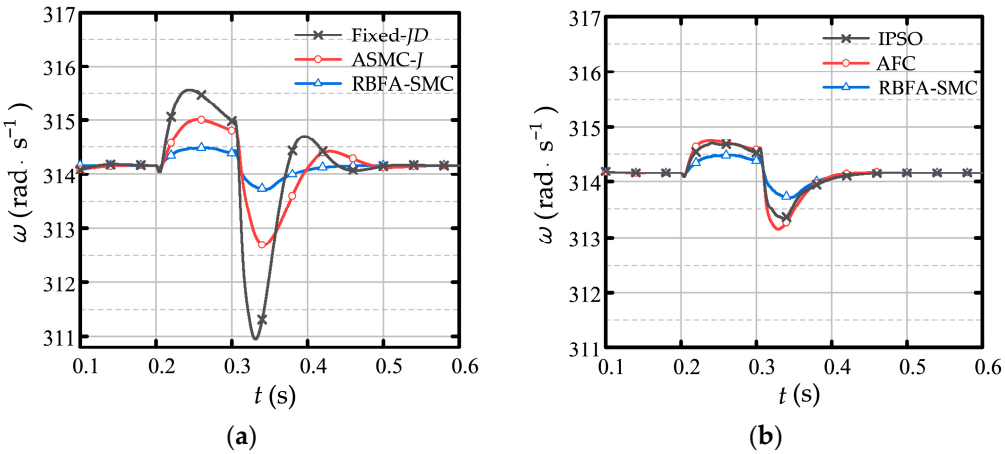


Figure 15. Comparison of angular frequency response under voltage sag conditions. (**a**) Longitudinal comparison; (**b**) Cross-sectional comparison.

As shown in Figure 15a, following a grid voltage dip, the VSG frequency increases due to excess active power. After fault clearance, a significant grid-connection fluctuation occurs, with the VSG frequency rapidly decreasing before recovering and eventually stabilizing at the rated value. Compared to the traditional Fixed-*JD* strategy and A-SMC strategy, the RBFA-SMC strategy exhibits a smaller maximum frequency deviation and a lower

rate of frequency change during the system voltage drop phase. It significantly mitigates frequency fluctuations and prevents the risk of instability.

Comparing the angular frequency responses under voltage sag conditions in Figure 15b reveals that the IPOS adaptive algorithm, AFC algorithm, and RBFA-SMC strategy all provide robust support for grid frequency. However, the IPOS adaptive algorithm exhibits irregular oscillations during frequency fluctuations. This is attributed to its high computational complexity and poor real-time performance, leading to mismatch phenomena. The AFC algorithm, however, suffers from insufficient adaptability of its fuzzy rule base, resulting in inadequate dynamic performance in terms of overall frequency response. The RBFA-SMC strategy proposed in this paper incorporates an RBF neural network to reduce system oscillations. By combining the advantages of two major control methods, it achieves higher stability and dynamic performance.

Table 4 compares the dynamic responses of active power under voltage sags for the Fixed-*JD* strategy, A-SMC strategy, and RBF-SMC strategy. After voltage restoration, the Fixed-*JD* strategy exhibited power overshoot of ΔP_1 = 17.26 kW, reduced to ΔP_2 = 13.44 kW under the A-SMC strategy. The RBF-SMC strategy, leveraging the robustness of sliding mode control, suppressed overshoot to ΔP_3 = 0.30 kW, with a smooth power curve free of oscillations.

Table 4. Indicators for analyzing different control strategies under voltage sag conditions.

Control Strategy	ΔP_{max} (kW)	$\Delta \omega_{max}$ (rad·s^{-1})	t_s (s)
Fixed-*JD*	17.26	3.19	0.36
ASMC-*J*	13.44	1.46	0.32
AFC	1.21	0.99	0.28
IPSO	0.29	0.81	0.25
RBFA-SMC	0.30	0.43	0.22

As shown in Figure 16a, all three control strategies exhibit significant power fluctuations following a grid voltage dip, particularly generating large inrush currents at the onset and conclusion of the dip. Under traditional control schemes, this may pose a risk of instability. Throughout the entire voltage dip process, the RBFA-SMC strategy dynamically adjusts power output to track voltage changes, enabling a smoother return to steady-state operation and facilitating grid integration.

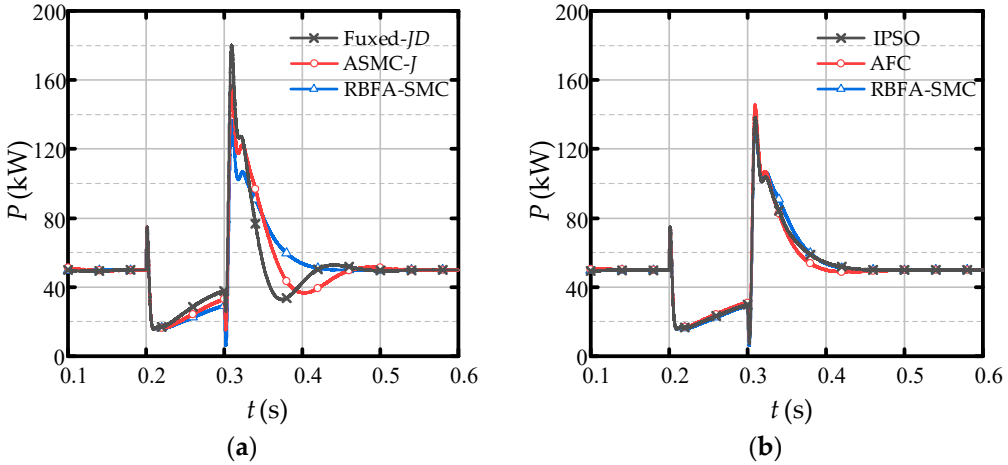


Figure 16. Comparison of active power responses under voltage sag conditions. (**a**) Longitudinal comparison; (**b**) Cross-sectional comparison.

Comparing active power responses during the voltage dip scenario in Figure 16b, the IPOS adaptive algorithm, AFC algorithm, and RBFA-SMC strategy exhibit consistent active power responses. All can adjust active power output in response to voltage fluctuations during grid voltage variations. Although inrush currents occur during disconnection and reconnection phases, they do not cause instability. During the final transient-to-steady-state transition phase, the RBFA-SMC strategy exhibits the smallest overshoot and a smoother transition process.

Figure 17 illustrates the dynamic variations in virtual inertia J and damping coefficient D under the RBFA-SMC strategy during system voltage sags. When voltage sags occur in the grid, the RBF neural network dynamically optimizes J and D based on the adaptive law. During voltage fluctuations, it supports system frequency to prevent instability risks, reduces the amplitude of transient fluctuations in VSG output frequency and active power, and further shortens the time required for the system to recover to steady state.

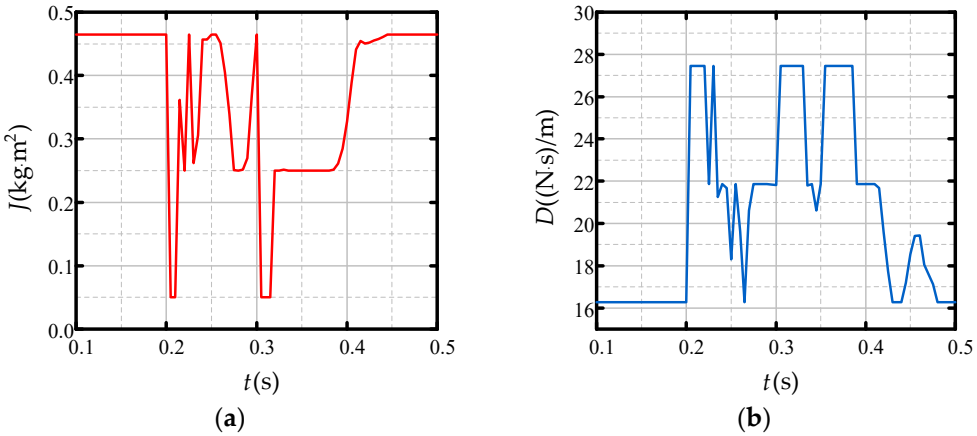


Figure 17. Under voltage sag conditions. (**a**) Real-time value of J; (**b**) Real-time value of D.

6. Conclusions

To address the insufficient transient performance optimization of current VSG due to multi-parameter cooperative adaptive challenges in sliding mode control, this paper proposes an RBF neural network adaptive sliding mode control strategy to enhance traditional VSG adaptive sliding mode control. By designing neural network weights with adaptive reaching rates for multiple parameters and cooperatively controlling virtual inertia and damping coefficients, the strategy avoids local optima traps. This enables more stable dynamic frequency processes and achieves more precise dynamic adjustments. To validate the effectiveness of the control strategy, this study simulated scenarios involving grid disturbances and intermittent operation of distributed power sources, establishing low-frequency ride-through and output fluctuation conditions. By comparing multiple VSG parameter control strategies under output power fluctuations, frequency transients, and voltage sags, the following conclusions were drawn:

1. The proposed RBFA-SMC strategy decouples and adaptively fits virtual inertia and damping coefficients via neural networks, effectively mitigating chattering issues in sliding mode control caused by parameter perturbations. It achieves multi-parameter cooperative adaptive adjustment, enhances the dynamic performance of transient processes, and resolves the issues of parameter coupling and dynamic instability inherent in traditional methods.
2. Under conditions of power output fluctuations, low-frequency ride-through, and voltage sags, the RBFA-SMC strategy reduces frequency overshoot by 56%, 51%, and 70.5%, respectively, compared to the A-SMC strategy. Active power fluctuations

decrease by 83%, 83%, and 97.7%, while transient recovery times shorten by 22.2%, 19%, and 31.2%, significantly enhancing system dynamic performance.

3. The mutual optimization of slip mode control and neural networks simultaneously suppresses instability issues caused by external disturbances and model uncertainties while avoiding the risk of getting stuck in local optima. Compared with IPOS adaptive strategies and AFC strategies, the proposed strategy in this paper further enhances dynamic performance and improves system robustness, validating its practical value in new power systems.

Author Contributions: Conceptualization, C.C.; methodology, J.S.; software, C.C.; validation, C.C. and H.W.; formal analysis, C.C.; investigation, C.C.; resources, J.S.; data curation, C.C.; writing—original draft preparation, C.C.; writing—review and editing, C.C.; visualization, J.S.; supervision, J.S.; project administration, H.W.; funding acquisition, J.S. All authors have read and agreed to the published version of the manuscript.

Funding: This work was supported by the National Natural Science Foundation of China, grant number 52277012.

Data Availability Statement: The original contributions presented in the study are included in the article; further inquiries can be directed to the corresponding author.

Conflicts of Interest: The authors declare no conflicts of interest.

References

1. Zhang, Y.; Yi, Y.; Li, L.; Zhong, K.; Li, Q.; Liu, S.; Xiao, H. Prospect of New Low-voltage Distribution System Technology Driven by Carbon Emission Peak and Carbon Neutrality Targets. *Autom. Electr. Power Syst.* **2022**, *46*, 1–12. [CrossRef]
2. Cao, W.; Qin, H.; Lu, J.; He, B.; Zhuang, K.; Li, G. Orientation and Application Prospect of Virtual Synchronous Generator in New Power System. *Autom. Electr. Power Syst.* **2023**, *47*, 190–207. [CrossRef]
3. Lv, Z.; Sheng, W.; Zhong, Q.; Liu, H.; Zeng, Z.; Yang, L.; Liu, L. Virtual Synchronous Generator and Its Applications in Micro-grid. *Proc. CSEE* **2014**, *34*, 2591–2603. [CrossRef]
4. Wang, Q.; Li, S.; Zeng, X. Control of T-type three-level inverter combined with VSG under voltage unbalance in source-containing distribution networks. *Electr. Mach. Control* **2025**, *29*, 65–73. [CrossRef]
5. Sui, S.; Zhao, T. Active disturbance rejection control for optoelectronic stabilized platform based on adaptive fuzzy sliding mode control. *ISA Trans.* **2022**, *125*, 85–98. [CrossRef]
6. Zhang, Y.; Guo, Z.; Zhang, L. Fractional-Order Virtual Synchronous Generator Control Strategy Based on RBF Neural Networks. *Proc. CSU-EPSA* **2025**, *37*, 101–108. [CrossRef]
7. Sun, Y.; Xu, D.; Yang, W.; Bi, K.; Yan, W. Adaptive terminal sliding mode backstepping control for virtual synchronous generators. In Proceedings of the 2020 IEEE 9th Data Driven Control and Learning Systems Conference (DDCLS), Liuzhou, China, 20–22 November 2020; IEEE: Liuzhou, China, 2020. [CrossRef]
8. Chen, S.; Sun, Y.; Han, H.; Shi, G.; Guan, Y.; Guerrero, J.M. Dynamic frequency performance analysis and improvement for parallel VSG systems considering virtual inertia and damping coefficient. *IEEE J. Emerg. Sel. Top. Power Electron.* **2022**, *11*, 478–489. [CrossRef]
9. Zhang, Z.; Zhao, J.; Zeng, Z.; Mao, L.; Zhang, Y. VSG virtual inertia and dynamic damping compensation adaptive control based on RBF. *Power Syst. Prot. Control* **2024**, *52*, 155–164. [CrossRef]
10. Yu, J.; Sun, W.; Yu, J.; Wang, Y. Virtual synchronous generator control of a grid-connected inverter based on adaptive inertia. *Power Syst. Prot. Control* **2022**, *50*, 137–144. [CrossRef]
11. Zhu, J.; Yuan, Y.; Liu, P.; Du, S.; Guo, X.; Yang, M.; Qu, Y. Active power oscillation suppression strategy for dual-VSG grid based on power differential term. *Electr. Mach. Control* **2024**, *28*, 177–188. [CrossRef]
12. Wang, Z.; Zhang, Y.; Cheng, L.; Li, G. Improved Virtual Synchronization Control Strategy with Multi-Parameter Adaptive Collaboration. *Power Syst. Technol.* **2023**, *47*, 2403–2414. [CrossRef]
13. Srikanth, M.; Kumar, Y.V.P. Improved Virtual Synchronous Generator-Based Control Scheme for Enhanced Transient Response in Microgrids. *Eng. Proc.* **2023**, *56*, 4. [CrossRef]
14. Suvorov, A.; Askarov, A.; Ruban, N.; Rudnik, V.; Radko, P.; Achitaev, A.; Suslov, K. An Adaptive Inertia and Damping Control Strategy Based on Enhanced Virtual Synchronous Generator Model. *Mathematics* **2023**, *11*, 3938. [CrossRef]
15. Sheir, A.; Sood, V.K. Enhanced Virtual Inertia Controller for Microgrid Applications. *Energies* **2023**, *16*, 7304. [CrossRef]

16. Šumiga, A.; Polajžer, B.; Ritonja, J.; Kitak, P. Controllability-Oriented Method to Improve Small-Signal Response of Virtual Synchronous Generators. *Appl. Sci.* **2025**, *15*, 8521. [CrossRef]
17. Alghamdi, B. Fuzzy Logic–Based Decentralized Voltage–Frequency Control and Inertia Control of a VSG-Based Isolated Microgrid System. *Energies* **2022**, *15*, 8401. [CrossRef]
18. Othman, M.H.; Mokhlis, H.; Mubin, M.; Ab Aziz, N.F.; Mohamad, H.; Ahmad, S.; Mansor, N.N. Genetic Algorithm-Optimized Adaptive Network Fuzzy Inference System-Based VSG Controller for Sustainable Operation of Distribution System. *Sustainability* **2022**, *14*, 10798. [CrossRef]
19. Guo, J.; Fan, Y. Adaptive VSG parameter control strategy based on improved particle swarm optimization. *Electr. Mach. Control* **2022**, *26*, 72–82. [CrossRef]
20. Gurski, E.; Kuiava, R.; Perez, F.; Benedito, R.A.S.; Damm, G. A Novel VSG with Adaptive Virtual Inertia and Adaptive Damping Coefficient to Improve Transient Frequency Response of Microgrids. *Energies* **2024**, *17*, 4370. [CrossRef]
21. Zhang, H.; Wang, T.; Wei, F.; Zhang, R.; Zhang, Q.; Liu, X.; Lu, H.; Wang, X.; Wang, X. Stability Enhanced Control of VSG Based on Adaptive Virtual Impedance by Frequency. *Power Syst. Technol.* **2025**, 1–10. [CrossRef]
22. Li, X.; Wang, Z.; Chen, Y.; Luo, D.; Luo, C.; Fu, Y.; Fu, J. Active frequency support strategy for new energy inverters based on virtual inertia fuzzy adaptive control. *Power Syst. Prot. Control* **2024**, *52*, 25–37. [CrossRef]
23. Yang, T.; Liao, Y.; Tang, M. Adaptive robust-sliding mode control strategy for improving stability of interconnected power system with virtual inertia of wind farm. *Electr. Power Autom. Equip.* **2020**, *40*, 223–232. [CrossRef]
24. Yan, B.; Wang, B. VSG control based on adaptive Terminal sliding-mode control method. *Electr. Power Autom. Equip.* **2018**, *38*, 140–146. [CrossRef]
25. Lin, J.; He, G.; Zhang, G.; Zhou, Z. VSG power oscillation suppression strategy based on adaptive fuzzy sliding mode compensation. *Renew. Energy Resour.* **2024**, *42*, 1083–1088. [CrossRef]
26. Yuan, C.; Bi, J.; Chen, H.; Hu, J.; Feng, Y. Adaptive sliding mode variable structure control for multi virtual synchronous machine systems. *Power Syst. Prot. Control* **2023**, *51*, 26–36. [CrossRef]
27. Li, H.; Zhang, X.; Wang, W.; Yu, H. Stochastic configuring networks based adaptive sliding mode control strategy to improving stability of SG-VSG paralleled microgrid. *Int. J. Electr. Power Energy Syst.* **2024**, *161*, 110–193. [CrossRef]
28. Yang, X.; Yao, F.; Hao, P.; Lu, H. Adaptive inertia control for VSG based on improved RBF neural network. *Electr. Meas. Instrum.* **2021**, *58*, 112–117. [CrossRef]
29. Yang, T.; Liao, Y. Coordinated control method of virtual inertia and virtual damping for interconnected power system with doubly-fed wind farm. *Electr. Power Autom. Equip.* **2020**, *40*, 92–100. [CrossRef]
30. Wang, Y.; Jin, T.; Weng, J. Improved Moment of Inertia Adaptive Control for Virtual Synchronous Generators. *China Meas. Test* **2025**, 1–6. Available online: https://link.cnki.net/urlid/51.1714.TB.20240325.1223.010 (accessed on 1 October 2025).
31. Gao, Z.; Zhao, J.; Yang, X.; Yao, F.; Fang, J. RBF-Based Adaptive Control Strategy of Rotational Inertia and Damping Coefficient for VSG. *Electr. Power Constr.* **2022**, *43*, 132–139. [CrossRef]
32. Yao, F.; Zhao, J.; Li, X.; Mao, L.; Qu, K. RBF neural network based virtual synchronous generator control with improved frequency stability. *IEEE Trans. Ind. Inf.* **2020**, *17*, 4014–4024. [CrossRef]
33. Wang, S.; Li, Z.; Sun, L. RBF Neural Network Adaptive Sliding Mode Control of Magazine. *J. Ordnance Equip. Eng.* **2021**, *42*, 208–212. [CrossRef]
34. Tang, Z.; Ma, F.; Pei, Z. Improved PSO-RBF neural network adaptive sliding mode control for quadrotor systems. *J. Beijing Univ. Aeronaut. Astronaut.* **2023**, *49*, 1563–1572. [CrossRef]

Disclaimer/Publisher's Note: The statements, opinions and data contained in all publications are solely those of the individual author(s) and contributor(s) and not of MDPI and/or the editor(s). MDPI and/or the editor(s) disclaim responsibility for any injury to people or property resulting from any ideas, methods, instructions or products referred to in the content.